Review of Scientific Instruments

RESEARCH ARTICLE | FEBRUARY 23 2024

Synthetic Mirnov diagnostic for the validation of experimental observations

C. Büschel ; R. Kleiber ; A. Könies ; M. Drevlak ; M. Borchardt ; K. Rahbarnia ;
H. Thomsen ; S. Vaz Mendes; C. Brandt ; J. Knauer ; K. J. Brunner ; Wendelstein 7-X Team

Check for updates

Rev. Sci. Instrum. 95, 023506 (2024)
https://doi.org/10.1063/5.0190619

View Online
Export Citation
CrossMark

04 March 2024 11:52:02

MCL
MAD CITY LABS INC.
www.madcitylabs.com
Nanopositioning Systems

Modular Motion Control
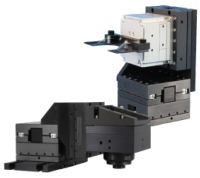
AFM and NSOM Instruments
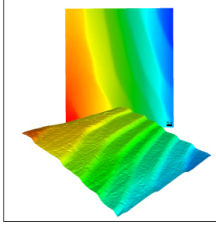
Single Molecule Microscopes
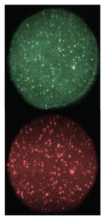
AIP Publishing

Review of Scientific Instruments ARTICLE pubs.aip.org/aip/rsi

Synthetic Mirnov diagnostic for the validation of experimental observations

Cite as: Rev. Sci. Instrum. 95, 023506 (2024); doi: 10.1063/5.0190619
Submitted: 7 December 2023 • Accepted: 24 January 2024 •
Published Online: 23 February 2024

View Online Export Citation CrossMark

C. Büschel,[a] R. Kleiber, A. Könies, M. Drevlak, M. Borchardt, K. Rahbarnia, H. Thomsen, S. Vaz Mendes, C. Brandt, J. Knauer, K. J. Brunner, and Wendelstein 7-X Team[b]

AFFILIATIONS

Max-Planck Institute for Plasma Physics, EURATOM Association, 17491 Greifswald, Germany

[a]Author to whom correspondence should be addressed: charlotte.bueschel@ipp.mpg.de
[b]See the authors list of T. Sunn Pedersen *et al.*, Nucl. Fusion **62**, 042022 (2022).

ABSTRACT

A synthetic Mirnov diagnostic has been developed to investigate the capabilities and limitations of an arrangement of Mirnov coils in terms of a mode analysis. Eight test cases have been developed, with different coil arrangements and magnetic field configurations. Three of those cases are experimental configurations of the stellarator Wendelstein 7-X. It is observed that, for a high triangularity of the flux surfaces, the arrangement of the coils plays a significant role in the exact determination of the poloidal mode number. For the mode analysis, torus and magnetic coordinates have been used. In most cases, the reconstruction of the poloidal mode number of a prescribed mode was found to be more accurate in magnetic coordinates. As an application, the signal of an Alfvén eigenmode, which has been calculated with a three-dimensional magnetohydrodynamics code, is compared to experimental observations at Wendelstein 7-X. For the chosen example, the calculated and measured mode spectra agree very well and additional information on the toroidal mode number and localization of the mode has been inferred.

© 2024 Author(s). All article content, except where otherwise noted, is licensed under a Creative Commons Attribution (CC BY) license (http://creativecommons.org/licenses/by/4.0/). https://doi.org/10.1063/5.0190619

04 March 2024 11:52:02

I. INTRODUCTION

Mirnov coils are widely used to measure magnetic field fluctuations and identify mode activity in fusion devices. Poloidal or toroidal arrays of Mirnov coils provide spatial–temporal resolution and offer the possibility to determine the poloidal mode number m or toroidal mode number n in addition to the frequency f of the mode. While the frequency resolution is given by the sampling rate and accuracy of the analysis tools, the spatial resolution depends also on the shape of the flux surfaces and the geometry of the coil array. The question is how to determine the structure of a mode that is propagating in the plasma with Mirnov coils located at the inner wall of the plasma vessel. There are different aspects that have to be taken into account: 1. Only a limited number of Mirnov coils can be installed in the plasma vessel. 2. In general, the geometry of the coil array differs from the shape of the flux surfaces, which depend on the magnetic field configuration. 3. The Mirnov coils are often non-uniformly spaced due to constructional constraints. 4. The mode's amplitude decays proportional to $r^{-(m+1)}$, with r being the distance to the magnetic axis and m being the poloidal mode number.[1] 5. In experiments, there can exist several modes at the same time, which probably couple with each other. Hence, the ability to determine the mode numbers with the Mirnov diagnostic depends on many different aspects.

Using a synthetic diagnostic, the capability of a Mirnov system can be estimated, and by the comparison with the calculated modes, the interpretation of experimental measurements is improved. There are different approaches with varying complexity. For example, for W7-AS, Zegenhagen *et al.*[2] used artificial data to investigate the capability of the installed Mirnov diagnostic with respect to different mode numbers, noise, as well as the superposition of modes. Bohlsen and Hole[3] proposed a Bayesian approach, modeling current distribution in a tokamak. Several diagnostics can be included in this analysis, such as Mirnov coils, soft x-ray diagnostics, and motional Stark effect diagnostics. However, the model has not yet been applied to experimental measurements. Focusing on the capabilities of the hardware and software of the Mirnov diagnostic, an end-to-end simulation has been developed by Testa *et al.*,[4] simulating $\delta\vec{B}$ directly at the Mirnov coil positions.

© Author(s) 2024

The synthetic Mirnov diagnostic presented in this paper calculates the signal of a mode at the Mirnov coil positions, taking into account the spatial discrepancy to the mode in the plasma. This work focuses on two main aspects: First, the effects of geometrical properties of the coil arrangement as well as the magnetic flux surfaces on the capability of the Mirnov diagnostic are investigated. These have to be taken into account for the comparison of experimental observations in different devices as well as for the comparison of observations in different magnetic field configurations in the same fusion experiment. Second, the Mirnov signal, which would be produced by an expected Alfvén eigenmode, is compared to experimental observations at the stellarator Wendelstein 7-X.[5,6] With this, the experimental mode with $f = 183$ kHz can be identified as an EAE (ellipticity-induced Alfvén eigenmode[7] with $\Delta m = 2$ and $\Delta n = 0$) localized in the outer region of the plasma.

This paper is structured as follows: In Sec. II, the implementation of the synthetic Mirnov diagnostic is presented. In Sec. III, eight test cases are investigated with varying coil arrangements and magnetic field configurations to analyze the capability of the Mirnov diagnostic in different geometrical configurations, including three experimental configurations of Wendelstein 7-X (W7-X). As the effects of geometrical configurations depend on the selected coordinate system, the analyses are done in torus and magnetic coordinates. In Sec. IV, a measured mode spectrum of a high performance W7-X plasma (20180918.041) is compared to the synthetic mode spectrum of an Alfvén eigenmode calculated by the three-dimensional magnetohydrodynamics (MHD) code CKA (**C**ode for **K**inetic **A**lfvén waves).[8] In Sec. V, the main results are summarized.

II. IMPLEMENTATION OF THE SYNTHETIC MIRNOV DIAGNOSTIC

The synthetic Mirnov diagnostic starts from a modeled eigenmode. For example, an ideal magnetohydrodynamic (MHD) eigenvalue code, e.g. CKA, provides a mode frequency ω and a mode structure given by the Fourier components of the perturbed parallel vector potential $\delta A_{\parallel mn}(s) \in \mathbb{C}$. The modes are defined in PEST coordinates[9] with the normalized toroidal flux $s \in [0,1]$ and the two angle-like coordinates in the poloidal and toroidal directions $\theta, \phi \in [0, 2\pi[$. The PEST coordinates are magnetic coordinates with straight magnetic field lines, where ϕ is equal to the usual cylindrical angle. The name PEST originates from a tokamak stability code named PEST.[10,11] The perturbed parallel vector potential can then be represented as

$$\delta A_\parallel = \sum_{(m,n)\in\mathscr{M}} \mathrm{Re}\left[\delta A_{\parallel mn}(s)\, \mathrm{e}^{\mathrm{i}(m\theta+n\phi)}\right], \tag{1}$$

where $\mathscr{M}$ is the set of Fourier modes taken into account. Here, only the parallel component of the perturbed vector potential is considered in accordance with the CKA code, used for the comparison with the experimental measurements in this paper. The associated magnetic field perturbation is given by

$$\delta\vec{B} = \nabla \times (\delta A_\parallel \vec{b}). \tag{2}$$

Hence, $\delta A_{\parallel mn}(s)$ is the basic ingredient from the numerical side. Two points should be noted: First, even if a mode with only one (m,n) component is specified, the coupling to the equilibrium inherent in Eq. (2) results in additional Fourier components in $\delta\vec{B}$. Second, the Fourier spectrum $F_{mn} = \max_{s\in[0,1]}(|\delta A_{\parallel mn}(s)|)$ depends on the specific coordinate system used. Nevertheless, the structure of F_{mn} serves as a theoretical guideline to classify a mode. For example, for a toroidal Alfvén eigenmode,[7] the two dominant components of F_{mn} differ by $\Delta m = 1$ and $\Delta n = 0$.

For calculating the signal measured by N Mirnov coils from the input mode, two main assumptions are made: First, the mode frequency ω is low enough that the quasi-electrostatic approximation is valid and the Biot–Savart law can be used ($\omega \ll c/a$, with c being the velocity of light and a being the minor radius). This is usually the case for the signals detected by a Mirnov system. Second, the magnetic field perturbation detected by the Mirnov coils stems from the current perturbation $\delta\vec{j} = \frac{1}{\mu_0}\nabla \times \delta\vec{B}$ inside an arbitrary control surface at the flux surface s_c. As the Mirnov coils are installed outside the plasma boundary, it would be convenient to choose $s_c = 1$, i.e., the last closed flux surface (LCFS). However, this is only possible, if the mode is the result of a free boundary calculation. Often MHD codes using fixed boundaries are employed because they are less complex, e.g. CKA. In this case, using a value close to one seems to be a reasonable choice.

After choosing s_c, the magnetic field perturbation at any point outside the control surface can be calculated from $\delta\vec{j}$ using the Biot–Savart law. This involves volume integrals and is numerically cumbersome. Employing the virtual casing principle,[12] the volume integral over $\delta\vec{j}(s)$ can be transformed into a surface integral over $\delta\vec{B}(s_c)$. For the synthetic Mirnov diagnostic, the code EXTENDER[13] is used, which is a numerical implementation of the virtual casing principle. It calculates the magnetic field perturbation $\delta\vec{B}(\vec{r}_l)$ at the Mirnov coil with number $l \in \{1, \ldots, N\}$ at the position $\vec{r}_l$ from the input $\delta\vec{B}(s_c)$.

The signal M_l at the lth Mirnov coil, with position $\vec{r}_l$, is calculated by $M_l = c_l\left(\delta\vec{B}(\vec{r}_l)\cdot\vec{n}_l\right)$, where $\vec{n}_l$ is the coil's normal vector. The constant c_l is given by the coil's technical design (e.g. winding number, area, sensitivity). In the following, the coil signals are combined in one vector $\vec{M} = \sum_{l=1}^{N} M_l\,\vec{e}_l$ consisting of N signals of the individual Mirnov coils, where $\vec{e}_l$ is the lth standard basis vector of $\mathbb{R}^N$.

Recalling Eq. (1), it is obvious that $\delta\vec{B}(s_c)$ only depends on

$$a = \delta A_{\parallel mn}(s_c) \quad \text{and} \quad a' = \frac{\partial}{\partial s}\delta A_{\parallel mn}\bigg|_{s=s_c}, \tag{3}$$

where the two independent quantities $a, a' \in \mathbb{C}$ are introduced for a short notation. For theoretical studies, it is convenient to specify an *ad hoc* set of a, a' and calculate the Mirnov signal. The whole chain from one input (m,n)-mode to its Mirnov signal can abstractly be written as $\vec{M} = \vec{\mathscr{T}}_{mn}(a, a')$, with a transfer operator $\vec{\mathscr{T}}_{mn}$. Since all operations necessary to arrive at the Mirnov signal from a prescribed mode are linear, the transfer operator has the properties $\vec{\mathscr{T}}_{mn}(a,a') = \vec{\mathscr{T}}_{mn}(a,0) + \vec{\mathscr{T}}_{mn}(0,a')$ and $\vec{\mathscr{T}}_{mn}(\alpha a + \beta b, 0) = \alpha\vec{\mathscr{T}}_{mn}(a,0) + \beta\vec{\mathscr{T}}_{mn}(b,0)$ for $\alpha, \beta \in \mathbb{R}$ [and analogously for $\vec{\mathscr{T}}_{mn}(0,a')$].

04 March 2024 11:52:02

© Author(s) 2024

Thus, the Mirnov signal for the mode in Eq. (1) can be written as

$$\begin{aligned}\vec{M} &= \sum_{(m,n)\in\mathscr{M}} \vec{\mathscr{T}}_{mn}(a,a') \\ &= \sum_{(m,n)\in\mathscr{M}} \big[\mathrm{Re}(a)\vec{\mathscr{T}}_{mn}(1,0) + \mathrm{Im}(a)\vec{\mathscr{T}}_{mn}(\mathrm{i},0) \\ &\quad + \mathrm{Re}(a')\vec{\mathscr{T}}_{mn}(0,1) + \mathrm{Im}(a')\vec{\mathscr{T}}_{mn}(0,\mathrm{i})\big], \end{aligned} \tag{4}$$

and pre-calculating the 4 $|\mathscr{M}|$ quantities $\vec{\mathscr{T}}_{mn}(1,0)$, $\vec{\mathscr{T}}_{mn}(\mathrm{i},0)$, $\vec{\mathscr{T}}_{mn}(0,1)$, $\vec{\mathscr{T}}_{mn}(0,\mathrm{i})$ allows for fast computation of the Mirnov signal for any input mode.

Now, it also becomes clear why it was not necessary to include the mode's time dependency in Eq. (1): It can be derived by using the properties of $\vec{\mathscr{T}}$. Assuming a time dependency $\delta A_{\parallel mn} \sim \mathrm{e}^{\mathrm{i}\omega t}$ leads to

$$\begin{aligned}\vec{\mathscr{T}}_{mn}(\mathrm{e}^{\mathrm{i}\omega t}a, \mathrm{e}^{\mathrm{i}\omega t}a') &= \frac{1}{2}\mathrm{e}^{\mathrm{i}\omega t}\big[\vec{\mathscr{T}}_{mn}(a,a') - \mathrm{i}\vec{\mathscr{T}}_{mn}(\mathrm{i}a,\mathrm{i}a')\big] \\ &\quad + \frac{1}{2}\mathrm{e}^{-\mathrm{i}\omega t}\big[\vec{\mathscr{T}}_{mn}(a^*,a'^*) + \mathrm{i}\vec{\mathscr{T}}_{mn}(\mathrm{i}a^*,\mathrm{i}a'^*)\big], \end{aligned} \tag{5}$$

with the asterisk denoting the complex conjugate. For the special case of a stationary wave, one gets

$$\begin{aligned}\vec{\mathscr{T}}_{mn}(\cos(\omega t)\,a, \cos(\omega t)\,a') &= \frac{1}{2}\mathrm{e}^{\mathrm{i}\omega t}\mathscr{T}_{mn}(a,a') \\ &\quad + \frac{1}{2}\mathrm{e}^{-\mathrm{i}\omega t}\mathscr{T}_{mn}(a,a'). \end{aligned} \tag{6}$$

In experiments, both types of waves can exist. Equation (5) describes a running wave with a clear propagation direction determined by the sign of the mode numbers. In contrast to this, a stationary wave, characterized by Eq. (6), has a symmetric mode spectrum. Because of their simpler behavior with respect to the Mirnov spectrum, in Sec. III, stationary waves are used.

In order to interpret experimental results, a poloidal angle θ_M and a toroidal angle ϕ_M are assigned to each Mirnov coil, using an operator $\mathscr{C}$. The Mirnov signal $\vec{M}$ is then transformed into $M(\theta_\mathrm{M}, \phi_\mathrm{M})$, defined on an irregular grid. A subsequent non-uniform Fourier transformation $\mathscr{F}$ finally gives the Mirnov spectrum $M_{m'n'} = \mathscr{F}\mathscr{C}\vec{M}$ (the range of m', n' is given by the number of coils and their geometrical arrangement). Hence, one (m,n) input mode gives rise to a whole Fourier spectrum in (m',n'). The workflow of the synthetic Mirnov diagnostic is shown in Fig. 1.

The prescription of assigning an angle to a coil is not unique, and thus, the Mirnov spectrum will look different for different choices of angles even though the Mirnov signal is independent of the coordinate system. It would be convenient to use magnetic coordinate systems, such as PEST or Boozer coordinates for the coil angles, but usually, these coordinates cannot be extended beyond the last closed flux surface (LCFS). Two procedures are applied to assign angles to the coils. The first simply uses torus coordinates (r,θ,ϕ). The second constructs a vector that is normal to the last closed flux surface and passes through the coil. The coil then gets assigned the PEST coordinate angles of the piercing point of this vector through the surface.

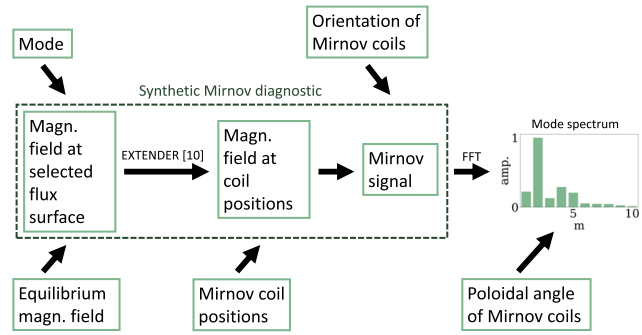

FIG. 1. Workflow of the synthetic Mirnov diagnostic.

To analyze the poloidal mode number, poloidal arrangements of Mirnov coils are commonly installed in experimental devices. Focusing on such an arrangement, the toroidal angle is constant and the Mirnov signal does not depend on the toroidal mode number. For simplicity, the toroidal mode numbers are defined by $n = 0$. Hence, it is most convenient to use PEST coordinates instead of the better known Boozer coordinates to keep the same toroidal angle for all Mirnov coils and make use of the two-dimensionality of the system.

This way, $M_{m'n'}$ only depends on m', which simplifies the subsequent analysis. When using the PEST coordinates, the whole transfer function from one input mode $(m_\mathrm{in}, 0)$ to the spectrum $(m_\mathrm{out}, 0)$ can be described by four complex transfer matrices $\mathscr{F}\mathscr{C}\vec{\mathscr{T}}_{m_\mathrm{in}0}(1,0)$, $\mathscr{F}\mathscr{C}\vec{\mathscr{T}}_{m_\mathrm{in}0}(\mathrm{i},0)$, $\mathscr{F}\mathscr{C}\vec{\mathscr{T}}_{m_\mathrm{in}0}(0,1)$, and $\mathscr{F}\mathscr{C}\vec{\mathscr{T}}_{m_\mathrm{in}0}(0,\mathrm{i})$ depicted in Fig. 2.

If these matrices have dominant diagonal entries, a direct assignment of the dominant peak in the mode spectrum to the poloidal mode number of the input mode m_input is possible. However, this is only the case for $\mathscr{F}\mathscr{C}\vec{\mathscr{T}}_{m_\mathrm{in}0}(0,1)$ and $\mathscr{F}\mathscr{C}\vec{\mathscr{T}}_{m_\mathrm{in}0}(0,\mathrm{i})$. The first two matrices $\mathscr{F}\mathscr{C}\vec{\mathscr{T}}_{m_\mathrm{in}0}(1,0)$ and $\mathscr{F}\mathscr{C}\vec{\mathscr{T}}_{m_\mathrm{in}0}(\mathrm{i},0)$, related to the mode's amplitude a, partly have strong off-diagonal components (especially $m_\mathrm{output} = 1$ components for $m_\mathrm{input} < 5$), giving rise to side peaks in the synthetic Mirnov spectrum, making the determination of m_input from the resulting mode spectrum difficult.

III. ANALYSIS OF DIFFERENT GEOMETRICAL ARRANGEMENTS

To investigate the effect of different arrangements of the Mirnov coils and magnetic field configurations on the capability to determine the poloidal mode number, eight test cases have been developed (see Fig. 3). The first case is a reference case with a generic circular tokamak equilibrium magnetic field with a plasma-beta of $\beta = 0\%$ (ratio of kinetic to magnetic pressure). The coil array consists of equally spaced coils, surrounding the cross section of the last closed flux surface. Cases 2 and 3 are with the same circular tokamak magnetic field configuration as the reference case but with different coil arrangements. For the remaining cases 4–8, the experimental magnetic field configurations EJM (cases 4 and 5), DBM (case 6), and FTM (cases 7 and 8) of W7-X are used. The three-letter code provides information about the so-called mirror ratio, defined as the toroidal field variation along the magnetic axis (first letter), the rota-

04 March 2024 11:52:02

© Author(s) 2024

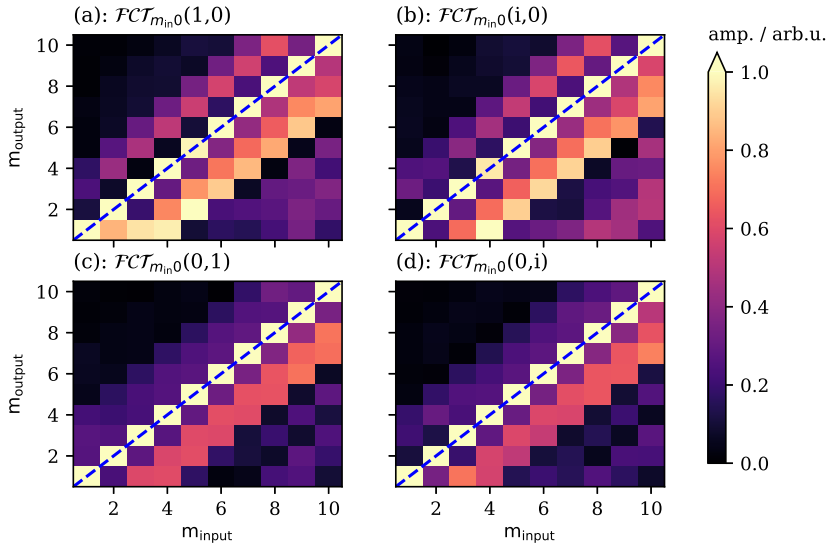

FIG. 2. Modulus of the entries of the transfer matrices, showing the output spectrum as a function of the input mode number for a standard W7-X configuration with the coil arrangement in half module 11. The amplitudes are normalized for each m_{input}. The diagonal components with $m_{output} = m_{input}$ are marked with blue dotted lines. The high amplitudes for other m_{output} indicate the sidebands in the mode spectrum and make the determination of the poloidal mode number difficult. For this configuration, the mode's amplitude gives rise to significant sidebands, especially for low m_{input}.

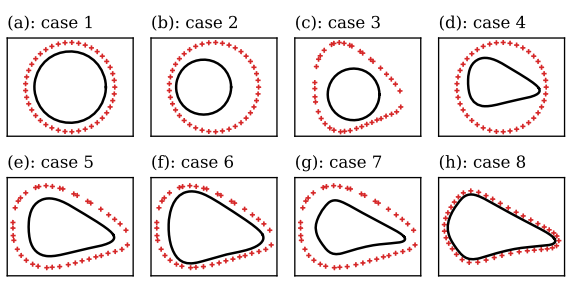

FIG. 3. Test cases with varying coil arrangements and magnetic field configurations. The magnetic field in cases 1–3 (a)–(c) is given by a generic tokamak equilibrium with $\beta = 0\%$. In cases 4–8, the magnetic field configuration is given by the standard configuration EJM [cases 4 (d) and 5 (e)], the low iota configuration DBM [case 6 (f)], and the high iota configuration FTM [cases 7 (g) and 8 (h)] of Wendelstein 7-X.

tional transform ι at the plasma boundary (second letter), and the horizontal shift of the plasma (third letter).[14,15] The three configurations chosen have no horizontal shift. While the EJM and FTM configurations have an intermediate mirror ratio, the DBM configuration has a comparable low mirror ratio. However, the main difference between the configurations is the rotational transform and its value at the LCFS ι_{LCFS}. The DBM configuration is referred to as a low-iota configuration ($\iota_{LCFS} = 5/6$), the EJM configuration is a so-called standard configuration (also with respect to the other two parameters, $\iota_{LCFS} = 5/5$), and the FTM configuration ($\iota_{LCFS} = 5/4$) is a high-iota configuration. The shape of the resulting flux surfaces of these configurations is shown in Fig. 3. Cases 5–7 reflect the experimental configurations of W7-X with the Mirnov coil array of half module 11 (HM11).

Since there are 41 Mirnov coils in HM11, all cases consist of 41 Mirnov coils for comparability. For a systematic analysis, analytical modes are used, consisting of one Fourier component to exclude effects from coupling between different Fourier components on the results. All prescribed modes have $n = 0$. The poloidal mode number m_{input} is varied to analyze the resolution of the poloidal mode number of the different cases. To reduce the amount of input parameters, the a and a' are chosen real valued, with $a = 1.0$ and $a' = -1.0$. As the resulting mode spectra are symmetric, only the positive side of the mode spectra will be shown in the following. A variation in these properties does not qualitatively change the results of the analyses presented in this section.

In order to check, if geometrical aspects affect the capability to determine the poloidal mode number of a prescribed mode m_{input} with the Mirnov diagnostic, the mode spectra are analyzed qualitatively. If the only significant peak in the mode spectrum is at m_{input}, the mode number of the prescribed mode can be clearly identified. However, the coupling to the equilibrium magnetic field can lead to additional peaks in the mode spectrum. In the following, the relation between the input mode's peak (IMP) and the first additional peak (FAP) is analyzed. The FAP is the largest peak in the spectrum besides the input mode's peak. Figure 4 visualizes three different relations between the IMP and the FAP. It shows the poloidal mode spectra in torus coordinates for case 1 with poloidal mode numbers $m_{input} = 2, 3, 4$ of the prescribed mode. These modes have been selected solely for illustration purposes. In Fig. 4(a), the IMP is clearly pronounced in the mode spectrum and the FAP has a significantly lower amplitude, while in Fig. 4(b), the $m = 2$ and $m = 4$ components are also pronounced. Although the highest peak in the mode spectrum is given by the IMP, without prior knowledge, one could falsely assume that the peaks at $m = 2$ and $m = 4$

04 March 2024 11:52:02

© Author(s) 2024

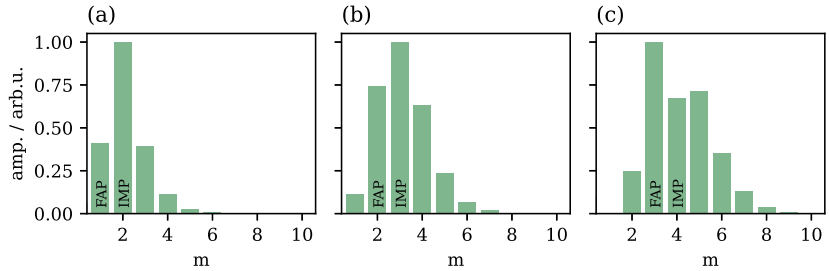

FIG. 4. Visualization of the mode spectra with differences in the dominance of the input mode's peak (IMP). While the IMP is clearly pronounced in (a), the first additional peak (FAP) has a significant amplitude in (b), and in (c), it dominates the spectrum. With increasing amplitude of the FAP [from (a) to (c)], the determination of m_{input} becomes more difficult. For this example, case 1 [circular tokamak, see Fig. 3(a)] with prescribed modes with $m_{\text{input}} = 2, 3, 4$ (a)–(c) has been applied. The mode spectra are in torus coordinates.

are caused by either further Fourier components of the mode or another mode in the plasma. In Fig. 4(c), the FAP has a higher amplitude than the IMP. In this case, the determination of the correct poloidal mode number is not possible without additional knowledge (e.g., theoretical predictions or other diagnostics in case of experimental measurements). In this paper, the focus is on modes with low poloidal mode numbers, as these are assumed to dominate the signals of the Mirnov coils due to the strong amplitude decay of modes with high poloidal mode numbers ($\propto r^{-(m+1)}$). Experimental measurements at W7-X confirm this assumption.[16]

Figure 5 shows the poloidal mode number of the highest peak in the mode spectrum $m_{1\text{st peak}}$ for the eight cases for prescribed modes with $m_{\text{input}} = 1, \ldots, 10$ in PEST [(a) and (b)] and torus coordinates [(c) and (d)]. The black lines indicate the poloidal mode number of the according IMP. For all cases, besides case 7, the IMP has the highest amplitude in the mode spectra in PEST coordinates. In contrast, only for cases 5 and 6, the IMP is the dominant peak in the mode spectra in torus coordinates for all m_{input}. Especially for cases 1–3 with a tokamak magnetic field configuration, it is not possible to determine the poloidal mode number of the prescribed modes from the mode spectra in torus coordinates. For the three experimental cases with W7-X configurations 5–7, there are no differences between the capability of PEST and torus coordinates to estimate the correct poloidal mode number of the prescribed mode. However, there is a significant difference for case 8 with the high iota magnetic field configuration of W7-X and an artificial coil arrangement adapted to the shape of the flux surfaces. While in PEST coordinates, the IMP is the first peak for all prescribed modes, in torus coordinates, $m_{\text{input}} = m_{1\text{st peak}}$ is only the case for $m_{\text{input}} < 5$. Since the IMP is much more pronounced in PEST coordinates than in torus coor-

04 March 2024 11:52:02

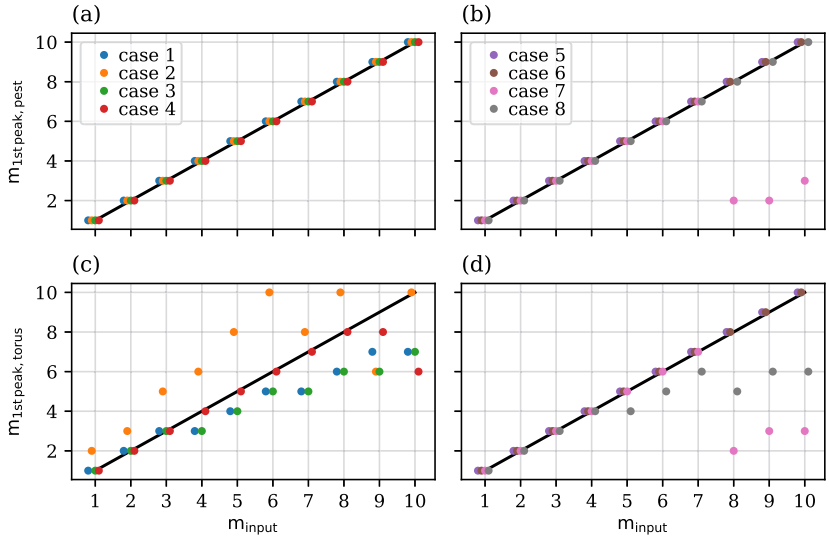

FIG. 5. Identifiability of the poloidal mode number for different prescribed modes in PEST and torus coordinates. Shown is the poloidal mode number of the highest peak in the mode spectra $m_{1\text{st peak}}$ for prescribed modes with $m_{\text{input}} = 1, \ldots, 10$ in PEST [(a) and (b)] and torus coordinates [(c) and (d)]. The black line indicates $m_{\text{input}} = m_{1\text{st peak}}$. Different colors of the dots show the different cases of Fig. 3 (cf. legend). Note that m_{input} is always a whole number. For visual separation of the different cases, the dots have been slightly shifted in the x-direction. For most cases, the poloidal mode number is more pronounced in PEST coordinates than in torus coordinates.

© Author(s) 2024

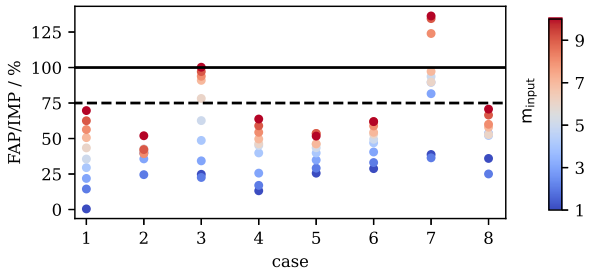

FIG. 6. Quality of the mode spectra in PEST coordinates depending on the prescribed mode. Relative amplitude of the FAP in the mode spectrum in PEST coordinates for modes with $m_{input} = 1, \ldots, 10$ (blue to red) with respect to the IMP for cases 1–8 (see Fig. 3). Although the IMP is clearly pronounced for all m_{input} for most cases, there are significant differences in the height of the FAP. In general, the FAP is higher for higher poloidal mode numbers.

dinates for most cases, the following investigations are done in PEST coordinates.

As mentioned before, even if the highest peak belongs to the IMP, there can be significant differences in the dominance of the IMP in the mode spectrum. In Fig. 6, the dominance of the IMP in the mode spectra in PEST coordinates is analyzed for the eight cases. For prescribed modes with $m_{input} = 1, \ldots, 10$ (blue to red), the amplitude of the FAP with respect to the IMP has been calculated. If the FAP is higher than 75% of the IMP (dashed line), the FAP would most likely be misinterpreted as another mode or another Fourier component of the mode in case of experimental measurements. If the FAP is even higher than the IMP (solid line), the determination of m_{input} is not possible anymore with the applied methods.

As already observed, case 7 is the only configuration, where the FAP has a higher amplitude than the IMP for the poloidal mode numbers $m_{input} = 8$–10. Apart from cases 3 and 7, the FAP always has an amplitude, which is less than 75% of the IMP for all poloidal mode numbers of the prescribed mode. Hence, m_{input} can be clearly determined. However, there are still significant differences between the cases. In general, it can be seen that additional peaks get more pronounced, if there are significant differences between the magnetic flux surface shape and the coil array geometry, as, for example, observed comparing cases 1 and 3 or cases 4 and 5. It should be noted that there are significant differences between cases 5 and 7, although the differences in the magnetic field configurations seem to be rather small (only the shape of the flux surface becomes more triangular). The same can be observed for differences in the coil arrangement for the high iota magnetic field configuration FTM of W7-X (cases 7 and 8). While the FAP is clearly pronounced in the mode spectra in case 7 for $m_{input} > 2$, its amplitude is less than 75% for all prescribed modes in case 8. In contrast, there are only small differences, if the magnetic field configuration EJM of W7-X is applied with either a circular coil array (case 4) or the coil arrangement of HM11 at W7-X (case 5). Seemingly for a triangular shape of the flux surfaces, the geometry of the coil arrangement plays a significant role in the correct determination of the poloidal mode number. For all cases, it can be seen that higher poloidal mode numbers have overall higher FAPs than low poloidal mode numbers.

Besides effects due to the geometry of the coil array and the flux surface shape, physical aspects of the AE itself play an important role in the capability of the Mirnov diagnostic to determine the poloidal structure of the mode. To investigate the effect of the $r^{-(m+1)}$-proportionality of the mode's amplitude decay, in Fig. 7,

04 March 2024 11:52:02

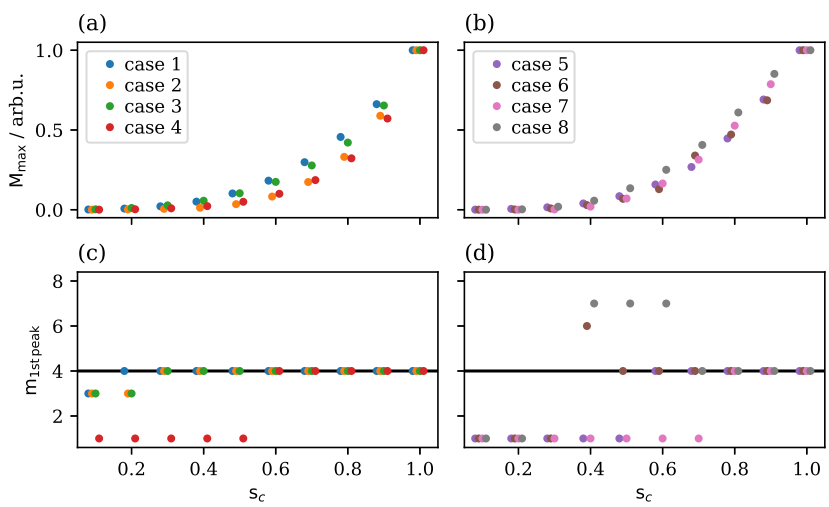

FIG. 7. Dependency of the maximum Mirnov signal and the correct determination of the poloidal mode number on the localization of the mode. Shown are the maximal Mirnov signal $M_{max}(s_c)$ normalized to $M_{max}(s_c = 1)$ [(a) and (b)] and the number of the dominant peak in the mode spectrum $m_{1st\,peak}$ in PEST coordinates [(c) and (d)], caused by a prescribed mode with $m_{input} = 4$ located at different toroidal flux surfaces s_c for cases 1–8. Note that the calculation is done for the same flux surface for all cases, and the shift of the dots in the x-direction is only for visualization purposes. For increasing distances between the mode and the Mirnov coils, the poloidal mode number gets less pronounced in the spectrum; around $s_c \sim 0.5$, the FAP dominates the spectrum.

© Author(s) 2024

the maximal Mirnov signal $M_{\max} = \max_{l \in [1,N]} M_l$ and the poloidal mode number of the dominant peak in the mode spectra in PEST coordinates are shown for a prescribed mode with $m_{\text{input}} = 4$ located at different toroidal flux surfaces s_c.

In all cases, $M_{\max}$ approximately follows the expected r^{-5}-decay. As can be seen in Figs. 7(c) and 7(d), the signal at the Mirnov coils becomes too small for a correct estimation of the poloidal mode number, if the distance between the mode and the Mirnov coils becomes too large. This is even more true when considering pickup noise in the coils, which is not considered here. For cases 1–3, the highest peak in the mode spectrum belongs to the IMP also for comparable large distances between the mode and the Mirnov coils, while for the W7-X magnetic configurations for $s_c \sim 0.5$, the FAP dominates the mode spectrum. Apart from cases 6 and 8, the FAP has a smaller poloidal mode number than the prescribed mode, when it has a higher amplitude than the IMP, showing that finer structures cannot be determined correctly. This effect increases even more with higher mode numbers.

Until here, the focus has been on modes with $m_{\text{input}} \leq 10$ as these are considered to dominate the Mirnov signal. Since 41 Mirnov coils are used for the eight test cases, according to the Nyquist limit, poloidal mode numbers up to $m_{\text{input}} = 20$ are expected to be resolvable. Strictly, the Nyquist limit is only applicable for equally spaced data points, but if there are only minor differences between the coil distances, the Nyquist limit is often still an appropriate estimate.[17]

However, for the Mirnov diagnostic, the distance between the mode and the coils complicates the analysis as explained before. As already shown in Fig. 5, the capability of the Mirnov diagnostic depends on the coil arrangement and the magnetic field configuration. Hence, the mode number resolution cannot be solely set by the number of Mirnov coils. In Fig. 8, the poloidal mode number of the first peak in the mode spectrum is shown for $m_{\text{input}} = 11, \ldots, 20$ for the eight test cases in PEST [(a) and (b)] and torus coordinates [(c) and (d)]. In contrast to low poloidal mode numbers, there are significant differences between the cases. As expected from Fig. 5, PEST coordinates are more appropriate than torus coordinates for the circular tokamak magnetic field configuration. However, also for the magnetic field configurations of W7-X, m_{input} is more pronounced in PEST than in torus coordinates for $m_{\text{input}} > 10$. Regarding PEST coordinates, there are noticeable differences between different coil geometries for the same magnetic field configuration, as can be seen for cases 1 and 2 for the tokamak magnetic field and for cases 4 and 5 for the EJM magnetic field configuration of W7-X. While the first peak in the spectrum still belongs to the IMP in cases 1 and 5, with coil geometries that are customized to the according magnetic field configuration, for most prescribed modes, m_{input} cannot be determined correctly for $m_{\text{input}} > 14$ for case 2 and $m_{\text{input}} > 15$ for case 4. Comparing these configurations, it gets clear that for higher poloidal mode numbers, an appropriate coil geometry gets even more crucial and large deviations of the distances between the LCFS and the Mirnov coils prohibit a clear determination of modes with high m.

In Table I, the capabilities of the Mirnov diagnostics of the eight test cases are summarized. For each case, the maximal poloidal mode number $m_{\text{input,max}}$ is given with $m_{1\text{st peak}} = m_{\text{input}}$ for all m_{input} with $m_{\text{input}} \leq m_{\text{input,max}}$. The highest resolution is obtained for the standard configuration and low iota configuration of Wendelstein 7-X with the coil arrangement in HM11. Although PEST coordinates have an overall higher resolution with respect to the poloidal mode number, it should be noted that for the three W7-X cases (cases 5–7), torus coordinates are also suited for mode numbers $m \leq 7$. In experimental measurements at Wendelstein 7-X, broad fluctuation bands around 200 kHz are observable with poloidal mode numbers

04 March 2024 11:52:02

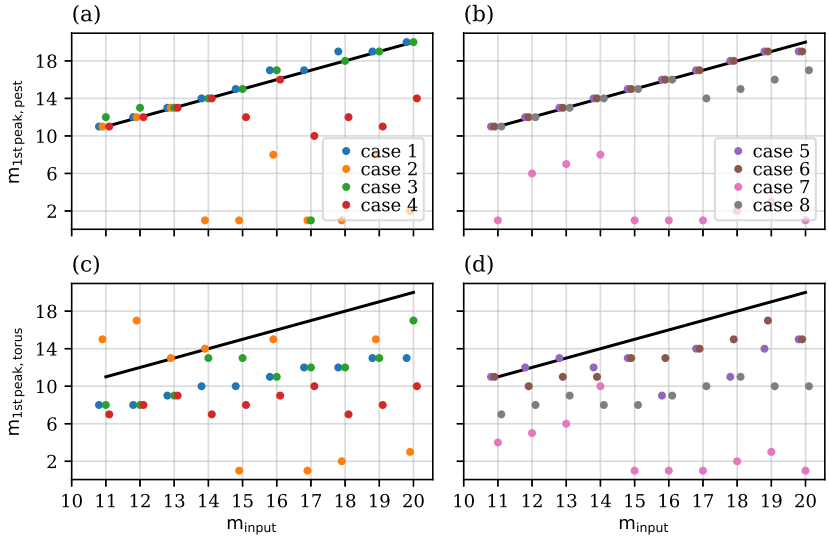

FIG. 8. Identifiability of the poloidal mode number for high m_{input} in PEST and torus coordinates. Shown is the poloidal mode number of the highest peak in the mode spectra $m_{1\text{st peak}}$ for prescribed modes with $m_{\text{input}} = 11, \ldots, 20$ in PEST [(a) and (b)] and torus coordinates [(c) and (d)]. Note that m_{input} is always a whole number, and the shift on the x axis is only for visual separation of the different cases. In contrast to Fig. 5, there are significant differences between the eight cases also for PEST coordinates.

© Author(s) 2024

TABLE I. Resolution in PEST and torus coordinates for the eight test cases. The first column gives the case number, the second column shows the arrangements of the Mirnov coils (see Fig. 3), and the last two columns are the resolution in PEST and torus coordinates, respectively. The resolution is given by the maximal poloidal mode number until which $m_{1\text{st peak}} = m_{\text{input}}$ with $m_{\text{input}} \leq m_{\text{input, max}}$. For all cases but case 7, the PEST coordinates have a higher resolution than torus coordinates.

Case	Configuration	$m_{\text{input,max}}$ PEST	$m_{\text{input,max}}$ torus
Case 1		15	3
Case 2		13	–
Case 3		10	3
Case 4		14	8
Case 5		19	13
Case 6		19	11
Case 7		7	7
Case 8		16	4

$m \leq 5$ in a large variety of magnetic field configurations.[16] Hence, torus coordinates might still be useful for the analysis, especially if observations are compared to other diagnostics that apply geometrical coordinates (as it is often done for radiation measurements, e.g., soft x-ray tomography[18]). Therefore, both coordinate systems are considered in Sec. IV, comparing experimental measurements to Mirnov signals of a calculated Alfvén eigenmode.

IV. COMPARISON OF A MEASURED AND A CALCULATED MODE

The synthetic Mirnov diagnostic has been applied to calculate the Mirnov signal of an Alfvén eigenmode to be compared to experimental measurements. The direct comparison of the resulting mode spectra goes one step further than mostly done for the comparison between the experiment and theoretical predictions, as this commonly ends with the identification of a calculated mode with a similar frequency and the same dominant Fourier components as observed in the experiment.[19–22] With the comparison between the numerical calculation and the measurement, the type of the AE and its toroidal mode numbers as well as its radial location can be estimated.

In this section, experimental observations at Wendelstein 7-X are compared to the calculations of the synthetic Mirnov diagnostic based on an Alfvén eigenmode calculated with the

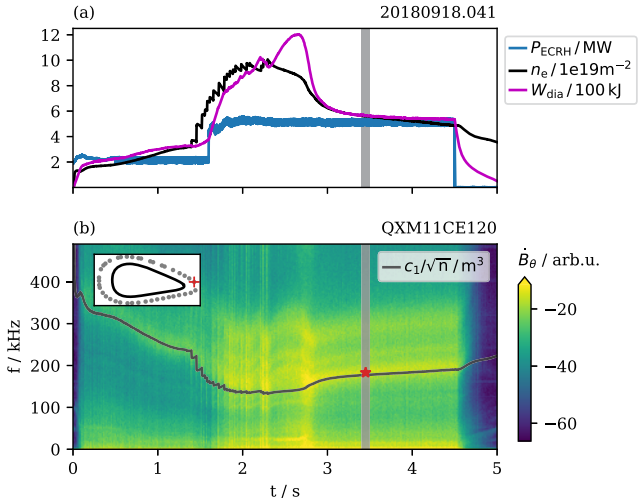

FIG. 9. High performance plasma 20180918.041. (a) Main experimental parameters: Electron cyclotron resonance heating (ECRH) power (blue), line-integrated electron density (black), and diamagnetic energy (magenta) for the experimental program 20 180 918.041 at W7-X. (b) Frequency spectrogram of the Mirnov coil QXM11CE120 (red cross in the inset) with $c_1/\sqrt{n_e}$ overlaid in black, with c_1 being a scaling constant. The frequency of the mode, analyzed in this section, is marked with a red star. In the inset, the Mirnov array in HM11 is shown (gray dots) with the LCFS of the magnetic configuration EJM (black line). The time interval, selected for the mode analysis, is marked with a gray bar in both figures.

CKA code. For the comparison, the experimental program 20180918.041 with the standard magnetic field configuration EJM has been selected. It is one of the so-called high performance programs of the operational phase 1.2 of W7-X in 2018, which are characterized by high densities and high diamagnetic energies of (transiently) more than 1 MJ.[6] This has been achieved by pellet fueling, where frozen hydrogen pellets are injected into the plasma to increase the central density.[23]

Figure 9(a) shows the external heating power P_{ECRH} (blue), provided by electron cyclotron resonance heating (ECRH),[24] the line-integrated electron density n_e[25] (black), and the diamagnetic energy W_{dia}[26] (magenta) for the experimental program 20180918.041. Multiple pellets have been injected in the time intervals from $t = 1.4$ s up to $t = 2.3$ s. At $t = 1.6$ s, the ECRH power is increased from $P_{\text{ECRH}} = 2$ MW to $P_{\text{ECRH}} = 4$ MW. Right after the last pellet injection, at $t = 2.4$ s, the diamagnetic energy strongly increases until it reaches its maximum of $W_{\text{dia}} = 1.2$ MJ at $t = 1.65$ s, denoting the high performance phase. Afterward, there is a strong decrease in the diamagnetic energy and the density. Both reach a quasi-constant level higher than before the pellet injection phase. During the time interval $t = 3.4$–3.5 s, selected for the mode analysis [gray bar in Fig. 9(a)], all parameters are approximately constant. In Fig. 9(b), the frequency spectrogram of the Mirnov coil QXM11CE120 in HM11 (red cross in the subplot) is shown. The broad fluctuation bands between 100 and 300 kHz follow a $1/\sqrt{n_e}$ development, clearly showing Alfvénic characteristics.

To determine the mode's frequency and poloidal structure, the SSI (**S**tochastic **S**ystem **I**dentification) method[27] and the FDD (**F**requency **D**omain **D**ecomposition) method[28] are applied.[29] The

04 March 2024 11:52:02

© Author(s) 2024

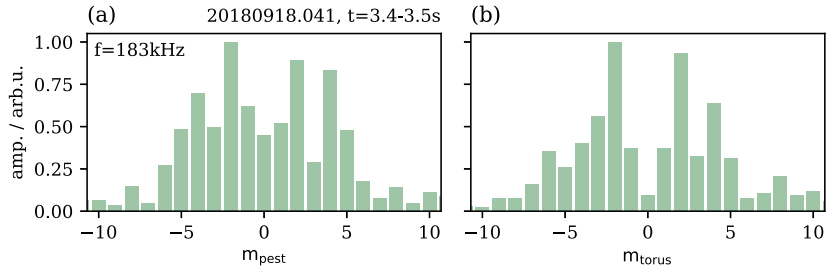

FIG. 10. Experimental mode spectrum in PEST (a) and torus coordinates (b). The poloidal mode spectrum is calculated from the mode structure of the experimental mode with f_{exp} = 183 kHz identified in the time interval t = 3.4–3.5 s in the experimental program 20180918.041. In both spectra, $m = \pm 2$ and $m = \pm 4$ are pronounced. However, the $m = 2$ component is more pronounced in torus coordinates and the $m = 4$ component is more pronounced in PEST coordinates.

poloidal mode spectrum is calculated either in PEST coordinates or in torus coordinates by a fast Fourier transformation of the mode structure, interpolated to equally spaced data points. A detailed explanation of the experimental mode analysis in W7-X is given by Rahbarnia *et al.*[30] The broad fluctuation band [see Fig. 9(b)] probably consists of several modes of low amplitude, which are difficult to be distinguished. A mode with f_{exp} = 183 kHz has been identified [red star in Fig. 9(b)] as the only clearly pronounced mode within this band.

In Fig. 10, the poloidal mode spectrum of the mode with f_{exp} = 183 kHz is shown in PEST and torus coordinates. In both mode spectra, the $m = \pm 2$ and $m = \pm 4$ components are pronounced. However, in torus coordinates, there are less additional peaks in the mode spectrum and the $m = |4|$ components are less pronounced. Similar observations have been made for modes in other experimental programs. Since the amplitudes for the positive and negative poloidal mode numbers are similar, the mode can be attributed as a stationary wave with no clear propagation direction.

To investigate if the experimental observations can be confirmed by theoretical calculations, the Alfvén continuum for the experimental program 20180918.041 at t = 3.4 s has been calculated with the CONTI code,[31] as shown in Fig. 11. The continuum branches are labeled with both signs for the mode numbers, as the CONTI code is based on ideal MHD. In ideal MHD, the dispersion relation only depends on the absolute value of the wave number; hence, there is no information about the sign of the mode numbers given .[32] Due to the convention used in CONTI, the poloidal and toroidal mode numbers of a continuum mode have opposite signs.[31] The calculation has been done with the slow sound approximation.[33] As input parameters, the equilibrium, calculated for the experimental program, and the measured density profile, provided by the Thomson scattering diagnostic,[35] have been used. For the equilibrium calculation the three dimensional MHD code VMEC[34] has been applied.

The appearance of two significant peaks in the mode spectrum, at $m = |2|$ and $m = |4|$, respectively, and its frequency indicate that the experimental mode is a gap mode with two dominant Fourier components.[7] In Fig. 11, the experimental mode's frequency f_{exp} = 183 kHz is indicated by a black line over all toroidal flux surfaces, as the measurements of Mirnov coils provide no information about the mode's radial localization.[1] The frequency lies in a gap of the Alfvén continuum. The continuum branch ($m = \pm 4$, $n = \mp 3$) crosses the gap at the outer region of the plasma. The continuum

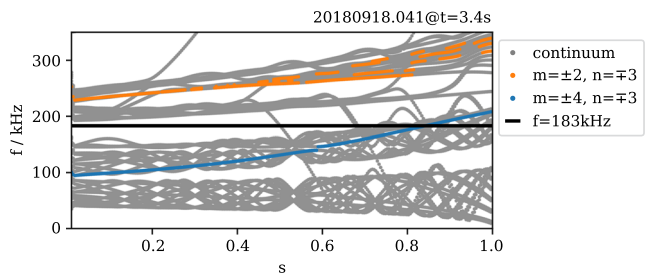

FIG. 11. Alfvén continuum for the experimental program 20180918.041 at t = 3.4 s. The continuum is calculated with the CONTI code[31] and based on the experimental magnetic field configuration and density profile. The two continuum branches $m = \pm 2$, $n = \mp 3$ (orange) and $m = \pm 4$, $n = \mp 3$ (blue) are colored. The frequency of the experimental mode f_{exp} = 183 kHz is marked with a black line.

branch ($m = \pm 2$, $n = \mp 3$) constitutes the upper border of another gap at higher frequencies. Although both branches cross different gaps, coupling is still possible, resulting in a so-called double-gap Alfvén eigenmode.[36] Thus, the experimental mode shows the characteristics of a double-gap EAE[7] with the dominant Fourier branches $m = |2|$, $n = |3|$ and $m = |4|$, $n = |3|$.

As the CONTI code only calculates the Alfvén continuum and not the gap modes, which can be excited and experimentally observed, the numerical code CKA is applied to identify an Alfvén eigenmode with the characteristics of the experimental mode. This mode is used as an input mode for the synthetic diagnostic to calculate the expected Mirnov signals. In this work, the ideal MHD version of the CKA code has been applied. The input parameters are the same as for the CONTI code, namely the VMEC equilibrium and the measured density profile at t = 3.4 s. The CKA code finds an Alfvén eigenmode with a frequency f_{CKA} = 219 kHz. The difference to the experimental frequency of f_{exp} = 183 kHz might be related to the fact that the mode is located in a broad fluctuation band. In Fig. 12, the radial distributions of the four dominant Fourier components of the calculated Alfvén eigenmode are shown.

It would be convenient to use the values of $\delta A_{\parallel mn}$ and $\delta A'_{\parallel mn}$ at the LCFS for the synthetic diagnostic. However, the CKA code assumes fixed boundary conditions, resulting in $\delta A_{\parallel}(s = 1.0) = 0$ for all Fourier components. Thus, as an input for the syn-

04 March 2024 11:52:02

© Author(s) 2024

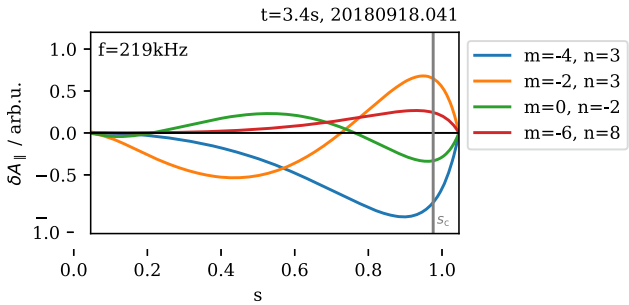

FIG. 12. Radial distribution of the four dominant Fourier components of an Alfvén eigenmode with a frequency f_{CKA} = 219 kHz. The calculation is done with the CKA code and based on parameters from the experimental program 20180918.041 at t = 3.4 s. For the calculation of the mode spectrum with the synthetic Mirnov diagnostic s_c = 0.93 is selected (gray line). The fixed boundary condition implemented in CKA causes $\delta A_{\|}(s = 1.0) = 0$.

thetic Mirnov diagnostic, s_c = 0.93 has been selected (gray line in Fig. 12), as it is still at the outer plasma region, but assumed not to be affected by the fixed boundary condition. For the calculation of the poloidal mode spectrum, the stationary wave model has been applied, as the experimental mode spectrum has a symmetric character (independent of the coordinate system, see Fig. 10), indicating that the experimental mode is a stationary wave.

In Fig. 13, the experimental mode spectrum in torus and PEST coordinates is compared to the mode spectrum calculated by the synthetic Mirnov diagnostic for the CKA mode in both coordinate systems. The experimental and synthetic Mirnov spectra are in reasonable agreement. The $m = |2|$ and $m = |4|$ components are clearly pronounced in the synthetic mode spectra based on the CKA mode in both coordinate systems. While in torus coordinates, the $m = |2|$ component has the highest amplitude, the $m = |4|$ component has a slightly higher amplitude in PEST coordinates. Due to the high similarities between the experimental and synthetic modes, the experimental observations can be attributed to an EAE with f = 219 kHz and $m_1 = |2|$, $n_1 = |3|$ and $m_2 = |4|$, $n_2 = |3|$ located in the outer region of the plasma.

V. CONCLUSIONS

In this paper, a synthetic Mirnov diagnostic has been presented, which calculates the signal of Mirnov coils caused by an Alfvén eigenmode, taking into account the spatial discrepancy between the mode and the Mirnov coils. The capability of the Mirnov diagnostic has been investigated for different prescribed modes using 8 test cases with varying coil array arrangements and magnetic field configurations (see Fig. 3). Two different coordinate systems have been considered, torus and PEST coordinates, with overall better results in PEST coordinates. However it should be note, that for low poloidal mode numbers, as expected to be dominately measured in experiments, torus coordinates performed as good as PEST coordinates.

Regarding geometrical properties, varying distances between the LCFS and the Mirnov coils (case 2) are only problematic for high poloidal mode numbers. Whereas differences in the magnetic flux surface shape and the coil arrangement cause additional peaks in the mode spectrum even for low poloidal mode numbers (case 3).

04 March 2024 11:52:02

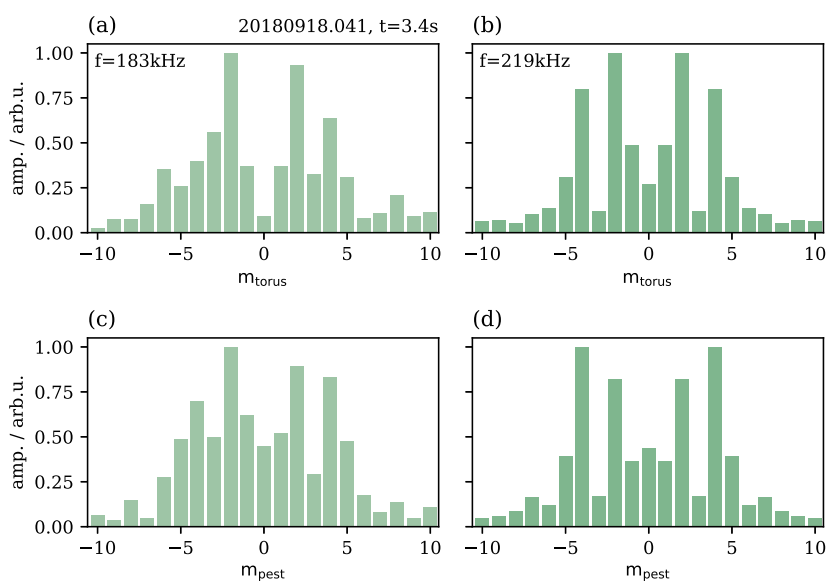

FIG. 13. Comparison between the experimental and modeled mode spectra in PEST and torus coordinates. Left: Poloidal mode spectrum in torus (a) and PEST coordinates (c) of an experimentally observed mode with f_{exp} = 183 kHz in the experimental program 20180918.041. Right: Poloidal mode spectrum in torus (b) and PEST coordinates (d) calculated by the synthetic Mirnov diagnostic for the CKA mode shown in Fig. 12. The main characteristics are the same in all spectra, e.g., pronounced $m = \pm 2$ and $m = \pm 4$.

© Author(s) 2024

It can be concluded that for strongly shaped flux surfaces (e.g., high triangularity), the geometry of the coil system plays an important role for the estimation of the correct poloidal structure of a mode. In general, the IMP is found to be more pronounced in the mode spectrum for similar shapes of flux surfaces and Mirnov geometry.

The sensitivity of the Mirnov diagnostic has been investigated with respect to properties of the prescribed mode. It has been shown that the higher the poloidal mode number, the less pronounced the IMP is in the calculated mode spectrum. Nevertheless, a clear determination of high m is still possible for some configurations (see Table I).

With respect to the radial location, it can be concluded, that the Mirnov signal is mainly given by modes having low poloidal mode numbers and propagating in the outer region of the plasma. Due to the $r^{-(m+1)}$-proportionality of the mode's amplitude, even for modes with low poloidal mode numbers ($m_{\text{input}} = 4$) located at $s_c < 0.5$, the Mirnov arrangements, considered in this paper, are not capable of correct determination of the poloidal structure for configurations with non-circular magnetic field configurations.

Using the CKA code with experimental parameters, an EAE has been identified and used as an input for the synthetic diagnostic for a comparison with an experimental mode. The analyses have been performed in PEST and torus coordinates. The main characteristics remain the same in both coordinate systems for the experimental and the calculated modes, namely dominant $m = |2|, |4|$ components as well as an overall symmetric character (see Fig. 13). Hence, the experimental observations can be assigned as an EAE with ($m_1 = |2|$, $n_1 = |3|$) and ($m_1 = |4|$, $n_1 = |3|$), which is located at the outer part of the plasma.

The example shown here is just proof of the principle. Nevertheless, the investigation of another experimental program showed comparably high similarities between the experimental mode spectra and the mode spectra of a calculated CKA mode. Since the Alfvén eigenmode activity is generally very weak in W7-X plasmas,[16,30] identifying clearly pronounced modes in the experimental programs is very challenging. In a future work, it would be convenient to model the Mirnov diagnostic of another device, where strong AE activity is observable in the experiments, e.g. TJ-II.[37]

Regarding experimental mode spectra, especially in the magnetic field configuration FTM, the mode spectra in torus coordinates are often more conclusive than the mode spectra in PEST coordinates. This is in clear contradiction to the general observation that PEST coordinates are more suitable for the majority of modes analyzed in Sec. III in different geometries of the flux surfaces and the coil arrangements, showing that the choice of an appropriate coordinate system is no easy task and should be taken serious, as it can significantly affect the results.

However, it also depends on the context which coordinates are more appropriate to apply. If, on the one hand, the focus is on a comparison of the experimental observations of different diagnostics, it is often more convenient to use torus coordinates, as for the analysis of the measurements of other diagnostics, torus coordinates or Cartesian coordinates are commonly applied, e.g., in the soft x-ray tomography diagnostic. In particular, if a first impression is needed during an experimental campaign, torus coordinates are useful as they are independent of the magnetic field configuration and can be used without having a calculation of the equilibrium available.

On the other hand, numerical simulations are mostly based on magnetic coordinates.[8,31] In this work, PEST coordinates have been applied in order to use the advantage that, in W7-X, all Mirnov coils are arranged in a poloidal plane. However, in the stellarator TJ-II, helical coil arrays with three-dimensional measurements are installed, and there, Boozer coordinates are applied for the mode analysis with poloidal and toroidal resolutions.[37] As mentioned before, the poloidal and toroidal mode numbers are always related to the specific coordinate system. Although these have been similar for torus and PEST coordinates in the analysis in Sec. III, this has to be taken into account, e.g., in the comparison of observations in different experimental devices as well as the overall capability of the Mirnov diagnostic, which has been shown to depend on geometrical properties.

The coil arrangement as well as the magnetic field configuration can be easily changed in the synthetic Mirnov diagnostic implementation, providing the possibility to study also experimental configurations of other stellarators as well as tokamaks. However, focusing on the calculation of poloidal mode spectra, the coil array has to be approximately in one toroidal plane. In the synthetic Mirnov diagnostic, the three-dimensional positions of the Mirnov coils are projected to the poloidal plane. Regarding the coil array of Wendelstein 7-X used for cases 3 and 5–7, the toroidal variation in the coil positions is small and does not affect the results.

Another important aspect is the possible misalignment of Mirnov coils with respect to the magnetic field. The artificial coil arrays of cases 1, 2, 4, and 8 are oriented to measure exactly the poloidal magnetic field component. Concerning the Mirnov array of W7-X, the normal vectors of the Mirnov coils installed in the experimental device have been used, which have small deviations from the exact poloidal orientation. This does not affect the mode analysis presented in this paper, and tests with small deviations from the poloidal orientation to the magnetic field of some coils for other test cases showed no significant effect on the results. However, a systematic analysis of the effect of misalignment of coil positions and orientations should be part of a future work, providing an assessment of misalignment thresholds, for which the one-dimensional mode analysis assumption remains justified.

Having a synthetic diagnostics, it is tempting to construct an inverse model. It has the advantage that the step of introducing coordinates to obtain a Mirnov spectrum will no longer be necessary. Instead, one can directly use the Mirnov signals as they are obtained from the experiment after applying the SSI code and, utilizing the synthetic diagnostics, try to find the coefficients of the model giving the best fit. These coefficients are directly amenable for comparison with code results. Such inverse models are usually ill conditioned, and it is then necessary to use a Bayesian approach or a regularization and variable selection method such as LASSO.[38] Investigations in this direction are currently undertaken and will be reported elsewhere.

04 March 2024 11:52:02

© Author(s) 2024

ACKNOWLEDGMENTS

This work was carried out within the framework of the EUROfusion Consortium, funded by the European Union via the Euratom Research and Training Programme (Grant Agreement No. 101052200—EUROfusion). Views and opinions expressed are, however, those of the authors only and do not necessarily reflect those of the European Union or the European Commission. Neither the European Union nor the European Commission can be held responsible for them.

AUTHOR DECLARATIONS

Conflict of Interest

The authors have no conflicts to disclose.

Author Contributions

C. Büschel: Conceptualization (lead); Data curation (equal); Formal analysis (lead); Investigation (lead); Methodology (lead); Validation (lead); Writing – original draft (lead). **R. Kleiber**: Conceptualization (supporting); Methodology (supporting); Software (lead); Writing – original draft (supporting). **A. Könies**: Software (equal). **M. Drevlak**: Software (equal). **M. Borchardt**: Software (equal). **K. Rahbarnia**: Data curation (equal); Supervision (equal); Writing – review & editing (equal). **H. Thomsen**: Writing – review & editing (equal). **S. Vaz Mendes**: Writing – review & editing (equal). **C. Brandt**: Writing – review & editing (equal). **J. Knauer**: Data curation (supporting). **K. J. Brunner**: Data curation (supporting).

DATA AVAILABILITY

The data that support the findings of this study are available from the corresponding author upon reasonable request.

REFERENCES

[1] M. Endler, B. Brucker, V. Bykov, A. Cardella, A. Carls, F. Dobmeier, A. Dudek, J. Fellinger, J. Geiger, K. Grosser, and W7-X Team, "Engineering design for the magnetic diagnostics of Wendelstein 7-X," Fusion Eng. Des. **100**, 468–494 (2015).

[2] S. Zegenhagen, A. Werner, A. Weller, and T. Klinger, "Analysis of Alfvén eigenmodes in stellarators using non-evenly spaced probes," Plasma Phys. Controlled Fusion **48**(9), 1333 (2006).

[3] N. Bohlsen and M. Hole, "A Bayesian formulation for perturbed current tomography in tokamaks," Plasma Phys. Controlled Fusion **65**(10), 105003 (2023).

[4] D. Testa, G. Ambrosino, M. Ariola, G. de Tommasi, and A. Pironti, "Development of algorithms for the end-end system simulation and performance analysis for a high-frequency magnetic diagnostic system: Application to ITER, JET and TCV," Fusion Eng. Des. **188**, 113406 (2023).

[5] G. Grieger, C. Beidler, E. Harmeyer, W. Lotz, J. Kißlinger, P. Merkel, J. Nührenberg, F. Rau, E. Strumberger, and H. Wobig, "Modular stellarator reactors and plans for Wendelstein 7-X," Fusion Technol. **21**(3P2B), 1767–1778 (1992).

[6] T. Klinger, T. Andreeva, S. Bozhenkov, C. Brandt, R. Burhenn, B. Buttenschön, G. Fuchert, B. Geiger, O. Grulke, H. P. Laqua, and W7-X Team, "Overview of first Wendelstein 7-X high-performance operation," Nucl. Fusion **59**(11), 112004 (2019).

[7] W. W. Heidbrink, "Basic physics of Alfvén instabilities driven by energetic particles in toroidally confined plasmas," Phys. Plasmas **15**(5), 055501 (2008).

[8] A. Könies, "A code for the calculation of kinetic Alfvén waves in three-dimensional geometry," in 10th IAEA TM on Energetic Particles in Magnetic Confinement Systems, Kloster Seeon, Germany, 2007.

[9] S. E. Kruger and J. M. Greene, "The relationship between flux coordinates and equilibrium-based frames of reference in fusion theory," Phys. Plasmas **26**(8), 082506 (2019).

[10] R. C. Grimm, J. M. Greene, and J. L. Johnson, "Computation of the magnetohydrodynamic spectrum in axisymmetric toroidal confinement systems," in *Controlled Fusion, Methods in Computational Physics: Advances in Research and Applications Vol. 16*, edited by J. Killeen (Elsevier, 1976), pp. 253–280.

[11] J. Manickam, R. C. Grimm, and R. L. Dewar, "The linear stability analysis of MHD models in axisymmetric toroidal geometry," Comput. Phys. Commun. **24**(3–4), 355–361 (1981).

[12] J. D. Hanson, "The virtual-casing principle and Helmholtz's theorem," Plasma Phys. Controlled Fusion **57**(11), 115006 (2015).

[13] M. Drevlak, D. Monticello, and A. Reiman, "PIES free boundary stellarator equilibria with improved initial conditions," Nucl. Fusion **45**(7), 731 (2005).

[14] J. Geiger, C. D. Beidler, Y. Feng, H. Maaßberg, N. B. Marushchenko, and Y. Turkin, "Physics in the magnetic configuration space of W7-X," Plasma Phys. Controlled Fusion **57**(1), 014004 (2014).

[15] J. Geiger, T. Andreeva, A. Dinklage, M. Hirsch, Y. Suzuki, H. Thomsen, G. Wurden, J. Alonso, C. Beidler, M. Beurskens, and W7-X Team, "Confinement and equilibrium with internal islands in a configuration scan with respect to iota in W7-X," in Proceedings of the 28th IAEA Fusion Energy Conf.(FEC-2020, Virtual Event), 2021.

[16] S. Vaz Mendes, K. Rahbarnia, C. Slaby, H. Thomsen, J. Schilling, M. Borchardt, R. Kleiber, A. Könies, J.-P. Bähner, A. von Stechow, and W7-X Team, "Broadband Alfvénic excitation correlated to turbulence level in the Wendelstein 7-X stellarator plasmas," Nucl. Fusion **63**(9), 096008 (2023).

[17] J. T. VanderPlas, "Understanding the Lomb–Scargle periodogram," Astrophys. J., Suppl. Ser. **236**(1), 16 (2018).

[18] C. Brandt, J. Schilling, H. Thomsen, T. Broszat, R. Laube, T. Schröder, T. Andreeva, M. N. A. Beurskens, S. A. Bozhenkov, K. J. Brunner, and W7-X Team, "Soft x-ray tomography measurements in the Wendelstein 7-X stellarator," Plasma Phys. Controlled Fusion **62**(3), 035010 (2020).

[19] N. N. Gorelenkov, E. D. Fredrickson, W. W. Heidbrink, N. A. Crocker, S. Kubota, and W. A. Peebles, "Discrete compressional Alfvén eigenmode spectrum in tokamaks," Nucl. Fusion **46**(10), S933 (2006).

[20] G. J. Kramer, R. Nazikian, B. Alper, M. de Baar, H. L. Berk, G.-Y. Fu, N. N. Gorelenkov, G. McKee, S. D. Pinches, T. L. Rhodes, and JET EFDA Contributors, "Interpretation of core localized Alfvén eigenmodes in DIII-D and Joint European Torus reversed magnetic shear plasmas," Phys. Plasmas **13**(5), 056104 (2006).

[21] Y. Kusama, G. J. Kramer, H. Kimura, M. Saigusa, T. Ozeki, K. Tobita, T. Oikawa, K. Shinohara, T. Kondoh, M. Moriyama *et al.*, "Characteristics of Alfvén eigenmodes, burst modes and chirping modes in the Alfvén frequency range driven by negative ion based neutral beam injection in JT-60U," Nucl. Fusion **39**(11Y), 1837 (1999).

[22] S. E. Sharapov, D. Borba, A. Fasoli, W. Kerner, L.-G. Eriksson, R. F. Heeter, G. T. A. Huysmans, and M. J. Mantsinen, "Stability of alpha particle driven Alfvén eigenmodes in high performance JET DT plasmas," Nucl. Fusion **39**(5), 699 (1999).

[23] J. Baldzuhn, H. Damm, C. D. Beidler, K. McCarthy, N. Panadero, C. Biedermann, S. A. Bozhenkov, K. J. Brunner, G. Fuchert, Y. Kazakov, and Wendelstein 7-X Team, "Pellet fueling experiments in Wendelstein 7-X," Plasma Phys. Controlled Fusion **61**(9), 095012 (2019).

[24] V. Erckmann, P. Brand, H. Braune, G. Dammertz, G. Gantenbein, W. Kasparek, H. P. Laqua, H. Maassberg, N. B. Marushchenko, G. Michel *et al.*, "Electron cyclotron heating for W7-X: Physics and technology," Fusion Sci. Technol. **52**(2), 291–312 (2007).

[25] K. J. Brunner, T. Akiyama, M. Hirsch, J. Knauer, P. Kornejew, B. Kursinski, H. Laqua, J. Meineke, H. Trimiño Mora, and R. C. Wolf, "Real-time dispersion interferometry for density feedback in fusion devices," J. Instrum. **13**(09), P09002 (2018).

[26] K. Rahbarnia, H. Thomsen, U. Neuner, J. Schilling, J. Geiger, G. Fuchert, T. Andreeva, M. Endler, D. Hathiramani, T. Bluhm, M. Zilker, B. B. Carvalho, A. Werner, and Wendelstein 7-X Team, "Diamagnetic energy measurement dur-

04 March 2024 11:52:02

© Author(s) 2024

ing the first operational phase at the Wendelstein 7-X stellarator," Nucl. Fusion **58**(9), 096010 (2018).
[27]P. Van Overschee and B. De Moor, *Subspace Identification for Linear Systems* (Springer, New York, 1996).
[28]R. Brincker, L. Zhang, and P. Andersen, "Modal identification of output-only systems using frequency domain decomposition," Smart Mater. Struct. **10**(3), 441 (2001).
[29]R. Kleiber, M. Borchardt, A. Könies, and C. Slaby, "Modern methods of signal processing applied to gyrokinetic simulations," Plasma Phys. Controlled Fusion **63**(3), 035017 (2021).
[30]K. Rahbarnia, H. Thomsen, J. Schilling, S. vaz Mendes, M. Endler, R. Kleiber, A. Könies, M. Borchardt, C. Slaby, T. Bluhm, M. Zilker, B. B. Carvalho, and Wendelstein 7-X Team, "Alfvénic fluctuations measured by in-vessel Mirnov coils at the Wendelstein 7-X stellarator," Plasma Phys. Controlled Fusion **63**(1), 015005 (2020).
[31]A. Könies and D. Eremin, "Coupling of Alfvén and sound waves in stellarator plasmas," Phys. Plasmas **17**(1), 012107 (2010).
[32]J. P. Goedbloed, "Once more: The continuous spectrum of ideal magnetohydrodynamics," Phys. Plasmas **5**(9), 3143–3154 (1998).
[33]M. S. Chu, J. M. Greene, L. L. Lao, A. D. Turnbull, and M. S. Chance, "A numerical study of the high-n shear Alfvén spectrum gap and the high-n gap mode," Phys. Fluids B **4**(11), 3713–3721 (1992).
[34]S. P. Hirshman, W. I. van RIJ, and P. Merkel, "Three-dimensional free boundary calculations using a spectral Green's function method," Comput. Phys. Commun. **43**(1), 143–155 (1986).
[35]E. Pasch, M. Beurskens, S. Bozhenkov, G. Fuchert, J. Knauer, R. C. Wolf, and W7-X Team, "The Thomson scattering system at Wendelstein 7-X," Rev. Sci. Instrum. **87**(11), 11E729 (2016).
[36]N. N. Gorelenkov, "Double-gap Alfvén eigenmodes: Revisiting eigenmode interaction with the Alfvén continuum," Phys. Rev. Lett. **95**, 265003 (2005).
[37]E. Ascasíbar, F. Lapayese, A. Soleto, A. Jiménez-Denche, A. Cappa, P. Pons-Villalonga, A. B. Portas, G. Martín, J. M. Barcala, R. García-Gómez *et al.*, "Measurements of magnetic field fluctuations in TJ-II plasmas with new in-vessel helical arrays of magnetic coils," Rev. Sci. Instrum. **93**(9), 093508 (2022).
[38]R. Tibshirani, "Regression shrinkage and selection via the LASSO," J. R. Stat. Soc.: Ser. B (Methodol.) **58**(1), 267–288 (1996).

04 March 2024 11:52:02

© Author(s) 2024